Atmos. Chem. Phys. Discuss., 12, 31955–31990, 2012
www.atmos-chem-phys-discuss.net/12/31955/2012/
doi:10.5194/acpd-12-31955-2012

Atmospheric Chemistry and Physics Discussions

A case study of the highly time-resolved evolution of aerosol chemical and optical properties in urban Shanghai, China

Y. Huang[1], L. Li[1], J. Li[1], X. Wang[1], H. Chen[1], J. Chen[1,2], X. Yang[1,2], D. S. Gross[3], H. Wang[4], L. Qiao[4], and C. Chen[4]

[1]Shanghai Key Laboratory of Atmospheric Particle Pollution and Prevention, Department of Environmental Science and Engineering, Fudan University, Shanghai 200433, China
[2]Research Institute for Changing Global Environment, Fudan University, Shanghai 200433, China
[3]Department of Chemistry, Carleton College, Northfield, MN 5507, USA
[4]Shanghai Academy of Environmental Sciences, Shanghai 200233, China

Received: 6 November 2012 – Accepted: 2 December 2012 – Published: 11 December 2012

Correspondence to: X. Yang (yangxin@fudan.edu.cn)

Published by Copernicus Publications on behalf of the European Geosciences Union.

Abstract

Characteristics of the chemical and optical properties of aerosols in urban Shanghai and their relationship were studied over a three-day period in October 2011. A suite of real-time instruments, including an Aerosol Time-Of-Flight Mass Spectrometer (ATOFMS), a Monitor for AeRosols and GAses (MARGA), a Cavity Ring Down Spectrometer (CRDS), a nephelometer and a Scanning Mobility Particle Sizer (SMPS), was employed to follow the quick changes of the aerosol properties within the 72-h sampling period. The origin of the air mass arriving in Shanghai during this period shifted from the East China Sea to the northwest area of China, offering a unique opportunity to observe the evolution of aerosols influenced by regional transport from the most polluted areas in China. According to the meteorological conditions and temporal characterizations of the chemical and optical properties, the sampling period was divided into three periods. During Period 1 (00:00–23:00, 13 October), the aerosols in urban Shanghai were mainly fresh and the single scattering albedo varied negatively with the emission of elemental carbon, indicating that local sources dominated. Period 2 (23:00 on 13 October to 10:00 on 15 October) was impacted by regionally transported pollutants and had the highest particulate matter (PM) mass loading and the lowest particle acidity, characterized by large fractions of aged particles and high secondary ion (nitrate, sulfate and ammonium) mass concentrations. Two sub-periods were identified in Period 2 based on the scattering efficiency of PM_1 mass. The comparison of these sub-periods highlights the influence of particle mixing state on aerosol optical properties. Period 3 (from 10:00 on 15 October to 00:00 on 16 October) had a low PM_1/PM_{10} ratio and a new particle formation event. We directly observed the influence of regionally transported pollutants on local aerosol properties and demonstrate that the PM mass extinction efficiency is largely determined by the chemical components and mixing states of the aerosol.

ACPD

12, 31955–31990, 2012

1 Introduction

Aerosol particles can scatter and absorb incoming solar radiation as well as outgoing thermal radiation, directly affecting the Earth's radiation budget and hence the global climate (Pöschl, 2005). The direct radiative forcing of aerosols is largely determined by their chemical components. Aerosols consisting mostly of inorganic materials (e.g. sea salt (Murphy et al., 1998; Li et al., 2011c), sulfate (Harris and Highwood, 2011), and nitrate (Nguyen et al., 2012)) and non-absorbing organic species (e.g. hydrophobic organic compounds (Maria et al., 2004)) tend to scatter light causing a "cooling effect," while those composed mostly of black carbon (BC) (Jacobson, 2001; Kopp and Mauzerall, 2010), soot (Zhang et al., 2008; Monge et al., 2010), mineral dust (Ramanathan et al., 2001; Lelieveld et al., 2002; Kaufman et al., 2005), and moderately absorbing organics (Andreae and Gelencsér, 2006; Sun et al., 2007; Wonaschütz et al., 2009; Yang et al., 2009) tend to be absorbing, exerting a "heating effect." According to their distributions of different chemical compositions, aerosols can be divided into external and internal mixtures, with the latter subdivided as homogeneous and heterogeneous mixtures, each of which has different interactions with light (Seinfeld and Pandis, 1998). Chemical compounds with different optical properties, coupled with complex mixing states, collectively increase the intricacies of aerosol and light interactions (Li et al., 2011b). There are growing needs to better understand and measure atmospheric aerosol optical properties.

Aerosols in the atmosphere evolve and participate in various physical and chemical modifications, e.g. coagulation, gas-to-particle partitioning, aqueous phase processing, and photochemical oxidation (Pöschl, 2005; Robinson et al., 2007; Jimenez et al., 2009). These reactions (also known as "aging") change the reactivity, hygroscopicity, volatility, and likely alter the optical properties of the aerosol (Lelieveld et al., 2002; Kanakidou et al., 2005; Adler et al., 2011; Cappa et al., 2011). To precisely trace the evolution of chemical and optical properties, simultaneous measurements of both chemical and optical properties with high time resolution are required. In the

ACPD
12, 31955–31990, 2012

past decade, online aerosol mass spectrometry has made significant contributions to studies of ambient aerosols, allowing particle composition to be correlated with rapid changes in environmental conditions (Pratt and Prather, 2012). For example, Moffet and Prather (2009) developed a single particle mass spectrometry method to simultaneously measure their mixing state and optical properties, concluding that when soot particles were coated by organic carbon or other secondary species, their absorption efficiency was enhanced by a factor of 1.6. Recently, Adler et al. (2011) combined a High-Resolution Aerosol Mass Spectrometer (AMS) and a White Light Aerosol Spectrometer (WELAS) to follow the chemical and optical evolution of biomass burning aerosols, finding a decrease in the overall aerosol absorption and scattering coefficients as the particles are aged through secondary organic aerosol processing. Cappa et al. (2012) used a suite of on-line instruments with high resolution to study the in situ absorption behavior of black carbon (BC) in different mixing states, demonstrating that after BC particles were coated with organic carbon through photochemical reactions, no significant absorption enhancement occurred. All these findings are possible due to the use of highly time-resolved chemical analyses.

With rapid economic growth and urbanization, mega-cities in China have experienced severe air pollution problems (Chan and Yao, 2008). Visibility degradation caused by enhanced aerosol concentration has become a pervasive phenomenon in the regions with dense population and fast industrialization (Wang et al., 2009a). Fine particles from anthropogenic emissions, either primary or formed through secondary processes, contribute the most to visibility impairment (Huang et al., 2012a; Yang et al., 2012). Sulfate, nitrate, ammonium, organic matter, and elemental carbon have been identified as the major chemical components in fine particles in Chinese mega-cities and contribute over 90 % of the extinction coefficient (Cao et al., 2012; Wang et al., 2012; Zhang et al., 2012a). However, although the aerosol optical properties were monitored in real-time, chemical analysis was performed off-line by collecting filter samples in most of the above studies and particle mixing state was not examined.

ACPD
12, 31955–31990, 2012

Our group has used the Aerosol Time-of-Flight Mass Spectrometer (ATOFMS) to measure the size and chemical composition of individual particles and their correlations with the fluctuation of gas phase pollutants and meteorological conditions in the urban area of Shanghai. The capabilities of this online single particle mass spectrometric method were proven essential to these studies (Wang et al., 2010; Huang et al., 2012d; Yang et al., 2012). Recently, we attempted to connect the evolution of the mixing state of carbonaceous particles with visibility degradation during haze episodes in Shanghai (Yang et al., 2012). In this paper, we deployed a series of high time-resolution instruments focusing on a 72-h period in which we studied the evolution of the properties of the urban aerosol in the Shanghai atmosphere. The aerosol properties we focus on here include single particle size and chemical composition, particle size distribution, bulk aerosol mass concentrations of water soluble inorganic ions, and optical properties (including scattering/absorption coefficient and single scattering albedo). As the fine particles (especially smaller than 1 µm) significantly affect atmospheric visibility (Seinfeld and Pandis, 1998), we will emphasize the influence of the evolution of various particle types and chemical species on the optical properties. This is the first report of highly time-resolved variations of aerosol optical properties associated with chemical compounds of single particle analysis in Shanghai.

2 Experimental

2.1 Single particle mass spectrometry

We used an ATOFMS (TSI 3800, Shoreview, MN, USA) to do single particle size and chemical analysis. Detailed information about the ATOFMS is available in previous publications (Gard et al., 1997; Wang et al., 2010). Briefly, aerosols in the size range of 0.2–2.0 µm are effectively drawn from the ambient atmosphere into the vacuum through an aerodynamic focusing lens (Liu et al., 1995a, b). The supersonic expansion accelerates the particles to a terminal size-dependent aerodynamic velocity. This

ACPD
12, 31955–31990, 2012

velocity is measured by two orthogonally oriented continuous lasers (532 nm) fixed at a set distance. Particle size is calculated from the measured speed using a calibration curve generated by monodisperse polystyrene latex spheres (Nanosphere Size Standards, Duke Scientific Corp., Palo Alto) with known diameters (0.22–2.00 µm). A pulsed desorption/ionization laser (Q-switched Nd:YAG laser, 266 nm) is fired when a particle arrives at the ion source region. Both positive and negative ions are analyzed simultaneously by the time-of-flight mass spectrometer. In this work, the power of the desorption/ionization laser was kept at ~ 1.0 mJ per pulse.

All single particle mass spectra acquired were converted into a list of peaks at each m/z using TSI MS-Analyze software with a minimum signal threshold of 30 arbitrary units above the baseline. The resulting peak lists were then imported into YAADA (version 2.11, www.yaada.org), a software toolkit in Matlab (version R2010b) for further analysis of particle sizes and chemical components. In this work, a total of 111 678 particles were chemically analyzed (with both positive and negative ion spectra) by the ATOFMS, accounting for about 18 % of all sized particles. Based on the similarities of the mass-to-charge ratio and peak intensity, particles were clustered by using the ART-2a (adaptive resonance theory) (Song et al., 1999) method with a vigilance factor of 0.85, a learning rate of 0.05 and 20 iterations. The resulting particle clusters were then grouped by hand into 11 general particle types according to mass spectral patterns. The grouped particles accounted for 92.9 % of all the particles with bipolar mass spectra. No significant temporal trend was found for the unclassified particles.

2.2 Monitor for AeRosols and GAses (MARGA)

A MARGA (ADI 2080, Applikon Analytical B. B. Corp., The Netherlands) with a $PM_{2.5}$ cyclone impactor was used to measure particulate water-soluble inorganic ions. The details of MARGA have been described previously (Jongejan et al., 1997; Li et al., 2010; Du et al., 2011; Makkonen et al., 2012). Briefly, MARGA is composed of two identical sampling boxes and an analytical box. The sampling box consists of two parts: one is a wet rotating denuder (WRD) for absorbing gas (HCl, HONO, SO_2, HNO_3, NH_3)

ACPD
12, 31955–31990, 2012

and the other is a steam jet aerosol collector (SJAC) for collecting particles (sampling efficiency of 99.7 %). Ambient air is drawn at the flow rate of 2 $m^3 h^{-1}$ through the WRD followed by the SJAC, respectively. The two liquid samples are dissolved in hydrogen peroxide solution and are temporarily stored in syringes (25 mL) in the analytical box. After filling the syringes for one hour, samples are then injected into the ion chromatograph (IC) in the analytical box. The IC is continuously controlled by an internal calibration method using a standard LiBr solution. In this work, only the mass concentrations of water-soluble inorganic ions (i.e. NH_4^+, Na^+, K^+, Ca^{2+}, Mg^{2+}, SO_4^{2-}, NO_3^-, Cl^-) in bulk particles were analyzed.

2.3 Optical measurements

A home built cavity ring-down spectrometer (CRDS) was combined with an integrating nephelometer (TSI 3563) and NO_x analyzer to monitor the optical properties of ambient aerosols. Detailed information about this optical measurement system has been reported (Li et al., 2011a). Briefly, two highly-reflective dielectric mirrors (540 nm center wavelength, 99.9985 % reflectivity, 6m radius of curvature, 0.8 in diameter, Los Gatos Research, Inc.) and a stainless steel cell with two aerosol inlets at both ends and one outlet in the middle formed the cavity. A 0.03 L min^{-1} flow of dry nitrogen is released near the mirrors to prevent particle contamination. The aerosol flow is set to 1 L min^{-1} with a filling length of 58 cm in the cavity while the entire distance between the two mirrors is 76.4 cm. A light pulse (532 nm, 100 μJ, duration 11 ns) produced by a Q-switched pulsed laser (CrystaLaser QG-532-500) is injected into the cavity. Then the intensity of light leaking through one of the mirrors is recorded by a Hamamatsu R928 photomultiplier. Typically 1000 ring-down traces are averaged to calculate the decay time. The extinction coefficient is determined by Eq. (1):

$$C_{\text{ext}} = \frac{L}{\text{lc}} \left(\frac{1}{\tau} - \frac{1}{\tau_0} \right) \quad (1)$$

ACPD
12, 31955–31990, 2012

where C_{ext} is the extinction coefficient of particles, L is the length of the cavity, "l" is the effective length occupied by particles, "c" is the speed of light, τ_0 is the ring-down time of the cavity filled with particle-free air, and τ is the calculated decay time.

The aerosol scattering coefficient and hemispheric backscattering coefficient is measured by an integrating nephelometer (TSI 3563) at three different wavelengths (450, 550, and 700 nm) with the flow of 5 L min^{-1}. Zero adjusting is done automatically every 2 h. Finally, the scattering coefficient is calculated at 532 nm ($\alpha_{scat,532}$) according to Eq. (2) (Anderson and Ogren, 1998):

$$\alpha_{scat,532} = \alpha_{scat,\lambda}\left(\frac{532}{\lambda}\right)^{-å} \quad (2)$$

where $\alpha_{scat,\lambda}$ is the scattering coefficient at the wavelength of λ and "å" is the Ångstrøm exponent. The single scattering albedo ω_0 is the ratio of the scattering coefficient to the extinction coefficient at a given wavelength (in this paper the default wavelength is 532 nm):

$$\omega_0 = \frac{\alpha_{scat}}{\alpha_{ext}} \quad (3)$$

The absorption (α_{abs}) and scattering (α_{scat}) coefficients combine to make the extinction coefficients (α_{ext}) according to Eq. (4):

$$\alpha_{ext} = \alpha_{abs} + \alpha_{scat} \quad (4)$$

2.4 Sampling period and site

The sampling lasted for 72 consecutive hours during 13–15 October 2011. The instruments were operated in the building of the Department of Environmental Science and Engineering, Fudan University (FDU, 31°14′ N, 121°29′ E) in urban Shanghai, close

ACPD
12, 31955–31990, 2012

to both residential and traffic emissions sources. Aerosols were transferred to the instruments through a 6 m long stainless steel pipe (45 mm inner diameter) with the inlet 2 m above the roof of the building. A cyclone pump was used to pull air through the sampling system at 30 L min^{-1}, minimizing particle residence time in the sampling line. Aerosols were dried by diffusion drying tubes before they reached the ATOFMS, MARGA, CRDS, and Nephelometer. The size distribution of the aerosol was monitored by a scanning mobility particle sizer (SMPS, TSI 3936) during the campaign. Local meteorological data including temperature, relative humidity (RH), wind speed and direction, and hourly averaged concentrations of PM_{10}, $PM_{2.5}$ and PM_1 were provided by the Shanghai Meteorological Bureau (temperature and RH seen in Fig. S1 in the Supplement).

3 Results and discussion

3.1 Overview of the meteorology

Backwards air trajectories were analyzed for each day using the HYSPLIT-4 (Hybrid Single-Particle Lagrangian Integrated Trajectory) Model developed by NOAA/ARL. 48-h back trajectories of each air mass at 100 m arrival height were computed every 6-h for each day ending at 16:00 UTC in Shanghai (GMT + 8). As shown in Fig. 1, the origins of air masses arriving at the sampling site changed dramatically during the sampling period. Local wind directions also changed, consistent with variation of the air mass. During almost the entire day of 13 October 2011, the air mass moved slowly from the East China Sea with an average wind speed of 3 m s^{-1}, bringing in clean air to the city. Daily average mass concentrations of PM_1 and PM_{10} were 17 and 21 µg m^{-3}, respectively. A drizzle started at 14:30 on 13 October and gradually developed to a heavy shower at around 22:00, causing a dip in the mass concentration of PM_1 (Fig. 2a). The rainfall stopped at around 04:00 on 14 October.

ACPD
12, 31955–31990, 2012

Coincident with the rainfall, starting at 23:00 on 13 October the wind direction changed from east to northwest. The air mass arriving at the sampling site travelled through Jiangsu Province and some industrial sites northwest of Shanghai, which are the most polluted areas in the Yangtze River Delta (Huang et al., 2012b, c), bringing in significant amounts of particulate pollutants. The PM_1 mass concentration increased steadily and reached a maximum value of 120 $\mu g\,m^{-3}$ at about 22:00 on 14 October. The high PM_1 loading lasted until around 10:00 on 15 October. From the latter half of 15 October, the air mass was transported over a long distance from the northwest of China. The average mass concentration of PM_{10} in this period was 76 $\mu g\,m^{-3}$. However, the mass ratio of PM_1 to PM_{10} was relatively low (the average value was 0.35), indicating an input of coarse particles. At midday on 15 October, a new particle formation event occurred (SMPS data in Fig 2a).

Based on the above analysis, we divided the entire sampling time into three time periods, summarized in Table 1. Period 1 (00:00–23:00, 13 October) is relatively clean with an air mass originating from the East China Sea; Period 2 (23:00, 13 October to 10:00, 15 October) is impacted by regionally transported pollutants from high emission zones. Period 3 (10:00–24:00, 15 October) is characterized by long-distance transport of coarse particles mixed with a new particle formation event. The quick change in meteorological conditions provided a good opportunity to trace the evolution of aerosols in the Shanghai urban area with highly time-resolved monitors.

3.2 Temporal variations of chemical and optical properties

3.2.1 Particle classification

Classification of particles analyzed by the ATOFMS can help to elucidate the origins, degree of aging, and mixing state of atmospheric aerosol particles. We classified 92.9 % of all hit particles into 11 groups according to their mass spectral characteristics. The names of these groups and their number fractions are shown in Table 2. The average mass spectral patterns of each group are shown in Figs. S2 and S3 in

ACPD
12, 31955–31990, 2012

the Supplement. The size distributions and temporal variation of the number fractions of these aerosol types are shown in Fig. 3. The difference between the definition of fresh and aged are the intensities of m/z −62 (NO_3^-) and −46 (NO_2^-) in the negative spectra, with the aged groups having stronger signals from both nitrate ions (Moffet et al., 2008). In addition, the appearance of the nitrate cluster at m/z −125 ($H(NO_3)_2^-$) indicates an excess of nitrate in all aged aerosol groups. More information about the size distributions of different particle types is presented in the supplementary materials.

In Period 1 when the air mass came from East China Sea, the total number of particles sized by the ATOFMS was relatively low. The number fractions of fresh OC and fresh biomass burning types accounted for as high as 60 %. Nearly constant particle numbers of the fresh biomass burning particles (shown in Fig. 3b) suggest some stable emission sources around, likely due to harvest-related activities. Compared with Periods 2 and 3, Period 1 had a larger number fraction of the EC type (4.2 % vs. 1.9 % for Periods 2 and 3) in average. The temporal profile of EC's number fraction had a distinct diurnal pattern peaking at 8:00 a.m. (as shown in Fig. 3c), due to the emission from commuter traffic. The freshness of the particles and the diurnal pattern of EC particles suggest that particles in Period 1 were mostly locally emitted.

From the beginning of Period 2, when the wind blew from the northwest, the raw particle counts detected by the ATOFMS jumped to about four times those seen in Period 1. Additionally, the aged particle types (aged biomass burning, OC, ECOC and ammonium) accounted for nearly 70 % in number fraction in Period 2, indicating that more organic species, ammonium and NO_x pollutants were transported to the sampling site. The fraction of aged OC particles generally exceeded the fresh type in Period 2. However, there was a burst for both the fresh OC and fresh ECOC particles occurred near 14:00 on 14 October followed by aged OC and aged ECOC peaks, suggesting the photochemical production of secondary organic aerosols. The time delay between the peaks of the fresh and aged types was about 8-h. Ammonium particles accounted for about 25 % of all observed particles and were nearly constant during the entire Period 2. In contrast, the number fraction of ammonium particles in Periods 1 and 3 stayed

ACPD
12, 31955–31990, 2012

less than 10 %. Two distinct peaks in ammonium particles occurred, with one at 00:00 on 14 October and the other around 12:00 on 4 October. The first peak was accompanied by high relative humidity (~ 94 %), while the second peak was consistent with the peak of sulfate/nitrate mass spectra and aged OC particles at noon on 14 October.

In Period 3, the number fraction of the fresh biomass type accounted for about 20 % of all particles. Additionally, the number fraction of the fresh OC type exceeded that of the aged OC type. This roller coaster transformation of fresh and aged OC clearly shows the evolution of aerosols from regional to local origins. The number fraction of ammonium particles varied similarly with the OC particles. As mentioned above, at the beginning of Period 3 an air parcel carrying coarse particles from the northwest arrived at Shanghai, as indicated by a low PM_1/PM_{10} value (35 %, compared with 78 % in Periods 1 and 2). However, no significant increase of dust particle number was recorded by the ATOFMS (observed dust particles only accounted for 2.0 %) because most dust particles exceeded its sampling size range. For the same reason, a new particle formation event was not observed by the ATOFMS, as the particles were below the sampling size range. The newly formed ultrafine particles and their impacts on aerosol optical properties will be discussed below. The temporal profiles of metal-containing and Na-K-rich particle types presented no significant spikes during the whole sampling period, suggesting local origins.

The discussion above reveals that the aerosol types and number concentration depend heavily on the source of the air mass arriving in Shanghai. This observation is consistent with previous studies that show the area to the northwest of Shanghai (i.e. the China Central Plain) is a very polluted region and that the regionally transported pollutants from there can cause a higher PM_1 loading in Shanghai (Huang et al., 2012a, c).

3.2.2 Water soluble inorganic ions in $PM_{2.5}$

Figure S4 in the Supplement shows the hourly resolved mass concentrations of $PM_{2.5}$ water-soluble inorganic ions in this experiment. Nitrate, sulfate, and ammonium

ACPD
12, 31955–31990, 2012

reached as high as 40, 35, and 23 $\mu g\,m^{-3}$, respectively, during the entire Period 2. These values were approximately 10 times higher than in other time periods, demonstrating the enhanced secondary production during this period, consistent with the observation from the classification of single particles. The mass concentrations of calcium and magnesium jumped suddenly from 0.3 and 0.08 $\mu g\,m^{-3}$ to about 1.2 and 0.18 $\mu g\,m^{-3}$, respectively, at the beginning of Period 3, corresponding to the time when the air parcel brought dust particles from the northwest of China. Water soluble potassium is often used as a tracer for biomass burning (Du et al., 2011). In this experiment, the mass concentration of water soluble K^+ varied from 2–4 $\mu g\,m^{-3}$. In Periods 1 and 2, the temporal profile of water soluble potassium agreed well (R^2 = 0.74) with that of biomass burning particle-counts from the ATOFMS, further confirming our particle classification. During the entire sampling period (Periods 1–3), K^+ correlated very well with chlorine (R^2 = 0.85), suggesting the presence of KCl-containing particles in the atmosphere. The water soluble inorganic ions show clearly that the regionally transported pollutants, especially ammonium, nitrate, and sulfate, have a strong influence on the composition of aerosols in urban Shanghai.

3.2.3 Profile of aerosol acidity

Sulfate, nitrate, and ammonium are usually considered to be secondary inorganic species in the atmosphere, related to human activity. As the major acids and the only base in the atmosphere, the ratio of sulfate and nitrate to ammonium, also called the particle acidity (He et al., 2012), can be used as a direct indicator to express the relative amount of acids and bases in the particulate phase. Particle acidity is an important parameter related to aerosol chemical and physical properties (Wang et al., 2010; Huang et al., 2012d). In the ATOFMS, particle acidity is defined as the ratio of the sum of absolute peak area of NO_3^- and HSO_4^- to that of NH_4^+ (Denkenberger et al., 2007). The inset in Fig. 4 shows that particle acidity is closely related to the particle size, and thus the size distribution of these three species could help us to clarify the

ACPD
12, 31955–31990, 2012

internal variation of particle acidity (see the discussion and Fig. S5 in the Supplement). The size-resolved particle acidity shows that the highest particle acidity appeared at ~0.28 µm, and as the particles grew, particle acidity declined. In a similar study by Denkenberger et al. (2007), the maxiuma paticle acidty occurred at the diameter of 0.16 µm, smaller than our observation.

The temporal variation of the ATOFMS particle acidity is plotted in Fig. 4. The color gradient from blue to red indicates the average size of aerosol particles observed with the ATOFMS. The black line is the equivalent charge ratio of major anions (SO_4^{2-} and NO_3^-) to cations (NH_4^+) from MARGA data (Makkonen et al., 2012). As with the size distribution of particle acidity from the ATOFMS, the high bulk particle acidity is consistent with small average particle size. Figure 4 shows the changes of particle acidity and size when the air masses arriving at Shanghai changed, consistent with the three time periods described in this study. During Period 1, particle size stayed relatively small and particle acidity was fairly high. In Period 2 particle acidity stayed relatively low and constant, while in Period 3 it was high again, especially during the new particle formation event, indicating that aerosols influenced by regionally transported pollutants from the northwest of Shanghai had lower particle acidities and larger particle sizes. Since MARGA can achieve quantitative detection of the concentration of soluble compounds in the particles, the highly-correlated temporal trends of the ATOFMS and MARGA results (R^2 = 0.82) confirms the validity of the particle acidity calculated from the ATOFMS data.

The equivalent charge ratio of [SO_4^{2-}] and [NO_3^-] to [NH_4^+] measured with the MARGA in Period 2 reached about 1.0, indicating that in the particle phase, ammonium almost completely neutralized nitric and sulfuric acid. The entirely neutralized conditions in the particle phase suggest the input of particulate ammonium in this episode. Departures from the acid-base ion balance, as seen in Periods 1 and 3, suggest that the local atmosphere is deficient in ammonia (Pathak et al., 2009; Wang et al., 2009b) while regional transport during Period 2 brings an ammonia- rich air mass to urban Shanghai. He et al. (2012) estimated the aerosol acidity of $PM_{2.5}$ in Beijing using these three inorganic

ACPD
12, 31955–31990, 2012

ions and found that the particles in the urban area were more acidic, consistent with our observations. Zhang et al. (2012b) also determined the aerosol acidity in several cities in China and suggested that most urban aerosols were substantially neutralized by local industrial NH_3 emissions. Since the cities they investigated are much smaller than the scales of Beijing and Shanghai, where there are no industrial estates releasing ammonia in the central urban area, their conclusion does not conflict with ours. When the air mass carried coarse dust particles to urban Shanghai in Period 3, particles stayed acidic. A low correlation coefficient between $[SO_4^{2-}]$ and $[Ca^{2+}]$ in Period 3 (observed over the entire sampling period) indicates that dust aerosols were of little importance in determining fine particle acidity.

3.2.4 Evolution of optical properties

The aerosol optical properties are summarized in Fig. 2. In Period 1, both the mass concentration of particulate matter (PM) and the extinction coefficient were fairly low. About 86 % of the PM mass loading was fine particles ($< 2.5\,\mu m$). A minimum in the single scattering albedo (~ 0.63) occurred at about 08:00 on 13 October, corresponding to the EC peak shown in Fig. 3b. The correlation coefficient between the EC particle number fraction and the single scattering albedo reached about −0.76, indicating a strong inverse relationship between them. During the rain at around 22:00 on 13 October, all the instruments detected its influence on atmospheric aerosols, showing a quick change of aerosol chemical and physical properties, as seen in Figs. 2 and 4. After the shower, the air was fairly clean with PM_1 levels of only $7.3\,\mu g\,m^{-3}$. The single scattering albedo at that time reached about 0.55, indicating that the absorption coefficient accounted for a significant fraction of extinction coefficient. However, no EC peaks were detected in individual particle mass spectra around that time. This could be explained by the increased number fractions of ultrfine particles (e.g. fresh EC particles) that are too small to be detected by the ATOFMS. The PM_1 mass concentration more than doubled in Period 2, as did the extinction and scattering coefficients, and stayed high until the beginning of Period 3. In Period 2, about 78 % of the PM_{10} mass

ACPD
12, 31955–31990, 2012

loading was due to particles with diameters smaller than 1 µm, compared with 35 % of that in Period 3. The extinction coefficient was always high during Period 2 while the single scattering albedo in this period actually showed two different patterns. The first 14-h in Period 2 had high single scattering albedo (~ 0.79) while from about 18:00 on 14 October it stayed at about 0.66. During the new particle formation event in Period 3, the values of PM_1 loading and the extinction coefficients were much lower, indicating a relatively clean air compared with Period 2.

3.3 Relationship between optical properties, PM_1, and chemical composition

The most direct effect of aerosols on people's senses is the degradation of visibility through absorption and scattering of light. The information from the number distribution of aerosols determined by the SMPS, hourly averaged PM_1 mass concentration, and the extinction (α_{ext}), scattering, and absorption coefficients and single scattering albedo recorded by the CRDS and the nephelometer were combined to investigate the variation of aerosol optical properties during this campaign (Fig. 2). Using a fixed observation wavelength (λ =532 nm), we will discuss two key parameters: PM mass loading and chemical composition. Note that relative humidity (RH) also has a profound impact on visibility (Chow et al., 2002a). In our experiment, aerosols passed through a diffusion drying tube before the measurement of optical properties, so the discussion excludes the influence of RH on the aerosol optical properties.

3.3.1 Relationship between PM_1 mass loading and extinction coefficient

Mie theory describes the absorption and scattering behavior of particles with particle sizes approximately that of the wavelength of incident light. As proved by previous studies, the highest particulate mass extinction efficiency lies in the size range of 0.1–1.0 µm, the range described by the PM_1 mass loading (Seinfeld and Pandis, 1998). As the particle size gets larger, the extinction efficiency is nearly dependent on D_p^{-1}. A tight linear correlation can be expected between PM_1 mass loading and extinction

ACPD
12, 31955–31990, 2012

coefficient (as shown in Fig. S6 in the Supplement). The correlations (R^2) between extinction coefficient and different PM mass loadings in the three time periods shown in Table 3 are consistent with the statement above. In order to check the contribution of PM mass in different size ranges ($PM_{1,1-2.5,2.5-10}$) in determining the aerosol extinction coefficient, size segregated PM mass loadings are also plotted in Fig. S6 in the Supplement. The distinct temporal trends of PM larger than 1 μm show that large particles had less impact on the extinction coefficient compared with PM_1.

The correlations between PM_1 and extinction coefficient in Periods 1 and 2 were much lower than that for Period 3, suggesting that the chemical composition and mixing state of the particles and their variations could also contribute to the extinction coefficient. A high R^2 could be an indicator of consistent chemical components or mixing state in the particle phase or a constant complex refractive index of the aerosol. Knowledge of PM mass loading alone cannot determine the extinction coefficients, given the observed effect of chemical composition.

3.3.2 Relationship between PM_1 chemical composition and extinction coefficient

To investigate the effects of different PM_1 chemical compositions on the extinction coefficient during these periods, we identified some consecutive hours in each time period which have nearly constant fractions of major particle types, as shown in Fig. 3c, and single scattering albedo temporal trends, as shown in Fig. 2c. Four new sub-periods were chosen with one in Period 1, two in Period 2 and one in Period 3, named Period 1a, 2a, b and 3a, respectively. The start and end time for each of these sub-periods is given in Table 1. Chemically-resolved size distributions of all particle types and raw particle counts in these four periods are shown in Fig. S7 in the Supplement. The linear fits of extinction coefficient versus PM_1 mass loading in each of these sub-periods are shown in Fig. 5a. The high correlations (R^2 = 0.90, 0.94, 0.88, and 0.93, respectively) are consistent with stable chemical and physical properties of the particles in these

ACPD
12, 31955–31990, 2012

time-periods, which are higher than the R^2 of the extinction versus PM_1 for the whole period, in all cases (Period 1: 0.65, Period 2: 0.61, and Period 3: 0.92, as shown in Table 3).

The value of the slope indicates the mass extinction efficiency of the particles. A larger slope means more effective extinction (Titos et al., 2012; Wang et al., 2012). In order to clarify the relative weight of scattering and absorption in the total extinction efficiency, we calculated linear fits of the scattering and absorption coefficients, respectively, with PM_1 mass loading (as shown in Table S1 and Fig. 5b). The values we calculated agree well with previously reported PM mass extinction efficiencies (Bergin et al., 2001; Chow et al., 2002b). The fraction of different particle types observed with the ATOFMS during these sub-periods is shown in Fig. 5b and the size distributions of the particles types in each sub-period is given in Fig. S7.

The scattering efficiency of Period 1a (1.41) was much smaller than that of Period 2a (4.31). A comparison of particle types observed in these two sub-periods (more aged OC and ammonium particles in Period 2a) indicates that ammonium and nitrate could be the causes of the larger scattering and extinction efficiencies in Period 2a. Period 1a and Period 3a both represent relatively clean local air conditions as discussed above. However, Period 3a had a higher extinction efficiency than Period 1a (4.87 vs. 2.04). Both the contributions of scattering and absorption effects on extinction efficiency were larger in Period 3a than in Period 1a, with the absorption fraction changing more dramatically. The difference of single scattering albedos in Period 1a and Period 3a, $\sim$0.70 and $\sim$0.62, respectively, was mainly caused by the increase in the aerosol's light absorption ability. The large number fraction of biomass burning particles (47 %) could be the reason for the high absorption efficiency in Period 3a (Adler et al., 2011). As discussed above, there was a new particle formation event in Period 3, but the ATOFMS could not follow the chemical evolution of the freshly formed particles. However, previous studies (Seinfeld and Pandis, 1998) have shown that for particles that absorb light, the mass absorption efficiency is nearly constant, independent of particle size, for particles with diameter less than 0.2 µm, and thus the newly formed small particles could

ACPD
12, 31955–31990, 2012

also contribute to the absorption efficiency in Period 3a. The higher number fractions of aged biomass burning and aged OC particles (containing more material such as secondary inorganic salts which scatter efficiently) in Period 3a could be the reason for its higher scattering efficiency compared with Period 1a.

The average single scattering albedos of Period 2a and b were 0.79 and 0.66, respectively. The lower extinction efficiency of Period 2b was mostly due to the much weaker particle light scattering ability (1.54 in Period 2b vs. 4.31 in Period 2a), while their light absorption ability only decreased a little (from 0.86 to 0.76) compared with Period 2a. Compared with the big differences in composition between Period 1a and 3a, Period 2a and b had nearly the same fractions of different particle types, as shown in Fig. 3c. The differential mass spectrum between particles in Period 2a and b (Fig. S8) shows that the particles in Period 2a contained more inorganic species (ammonium, nitrate, and nitrate cluster) and metals (i.e. potassium, iron, and lead), while the relative intensities of organic ion signals (i.e. $C_2H_3^+$, $C_2H_5^+$, C_3H^+, $C_2H_3O^+$) were ~20 % stronger in Period 2b. The transition between Period 2a and b occurred at around 14:00 in 14 October, the same time that the peaks of fresh OC and OCEC were observed, suggesting that secondary organic species formed in photochemical reactions could have changed the aerosol mixing state thereafter. Also, the OC/EC ion ratio (Spencer and Prather, 2006) was calculated as a function of size in single particles for these two periods (Fig. S9 in the Supplement). Though the two periods had almost the same number fraction of carbonaceous particles (91.2 % and 91.9 % of all detected particles, respectively), particles in Period 2b had a higher OC/EC ratio in the large size range (> 500 µm). The comparisons here suggest that the secondary organic material coating could lead to a smaller scattering efficiency. Recently, Adler et al. (2011) reported an observation of chemical aging altering aerosol optical properties, in which freshly emitted biomass burning particles became less absorbing after the addition of SOA. In our experiment, most particles in Period 2a were already deeply aged, containing secondary inorganic materials like sulfate and nitrate salts with strong scattering ability.

ACPD
12, 31955–31990, 2012

The further chemical aging process (SOA formation) in Period 2b covered the particle surfaces with less scattering materials.

In long term bulk measurements, mass fractions of sulfate, nitrate, and ammonium have been the focus when studying the contribution of chemical composition to the aerosol's extinction (scattering) coefficient (Cao et al., 2012; Wang et al., 2012; Zhang et al., 2012a). However, in a highly time resolved short term experiment like this, average mass fractions cannot offer as much information. Figure 5c shows the fraction of the average mass concentrations of SO_4^{2-}, NO_3^-, and NH_4^+ in $PM_{2.5}$ in the four sub-periods. The relative distribution of these species was nearly the same in all four sub-periods. Particles in Period 2a and b had almost the same mass fraction of these three species while they had distinct extinction behaviors. This suggests the importance of knowing the particles' mixing state in determining their extinction ability, as discussed above.

The four sub-periods discussed above were characterized by different particle mixing states and chemical components and hence distinct optical properties. In each sub-period, a good correlation between PM_1 mass loading and extinction coefficients was observed because of the constant chemical composition and mixing state of the particles, facilitating the prediction of bulk aerosol optical properties. Particles falling in the intervals between these sub-periods were in transition regimes, which caused the worse correlation coefficients for entire sampling period (as shown in Table 3). Our studies reveal that the highly time-resolved chemical analysis of aerosols can ensure more precise interpretations of aerosol optical properties, compared to the analysis solely based on meteorology and bulk chemical measurements.

4 Conclusions

Using high-time-resolution instruments, we investigated the evolution of the chemical and optical properties of PM_1 in the Shanghai urban area during a 72-h sampling period. We divided the study into three time periods based on the meteorological

ACPD
12, 31955–31990, 2012

conditions. Period 1 represented the typical local air conditions; during Period 2 local aerosols were influenced by regionally transported particles; and Period 3 included a fast long-range transport of coarse dust particles with few fine particles, as well as a new particle formation event. A detailed investigation of the temporal variation of the 11 particle types observed with the ATOFMS revealed that, during regional transport, aerosols were more aged and the ammonium particles increased dramatically. The increase in the mass concentrations of water soluble inorganic ions demonstrated the input of secondary inorganic species (sulfate, nitrate, and ammonium). The northwest air mass advection brought with it a great deal of ammonium to Shanghai, lowering the particle acidity in Period 2. Also, regional transport of pollutants greatly increased the extinction coefficient compared to local aerosols, as shown in Period 2.

To investigate the impacts of particle mass concentrations and chemical components on the aerosol optical properties, four sub-periods, during which the particle chemical composition and single scattering albedo stayed constant, were picked out of these three time periods. The correlations between the extinction coefficient and PM_1 mass loading in these sub-periods showed much better linearity compared to the rest of the sampling period. The comparisons of the chemical composition among the four sub-periods based on single particle analysis shows that: (1) nitrate and ammonium strongly increase the particle scattering efficiency; (2) a coating of secondary organic material might cause the decreased scattering efficiency of particles containing secondary inorganic materials like sulfate and nitrate salts. Our observations demonstrate that the highly time-resolved analysis of particle mixing state can help us have a better understanding of aerosol optical properties. In the current study, all the experiments were carried out under dry conditions. The influences of relative humidity on aerosol mixing state and the resulting optical property changes should be considered in future studies.

ACPD
12, 31955–31990, 2012

Supplementary material related to this article is available online at: http://www.atmos-chem-phys-discuss.net/12/31955/2012/acpd-12-31955-2012-supplement.pdf.

Acknowledgements. This work was supported by The National Natural Science Foundation of China (20937001, 21177027, 41275126) and the Science and Technology Commission of Shanghai Municipality (12DJ1400102, 10JC1402000). D. G. acknowledges support from Carleton College's Chang-Lan Faculty Development Fund.

References

Adler, G., Flores, J. M., Riziq, A. A., Borrmann, S., and Rudich, Y.: Chemical, physical, and optical evolution of biomass burning aerosols: a case study, Atmos. Chem. Phys., 11, 1491–1503, doi:10.5194/acp-11-1491-2011, 2011.

Anderson, T. L. and Ogren, J. A.: Determining aerosol radiative properties using the TSI 3563 integrating nephelometer, Aerosol Sci. Tech., 29, 57–69, doi:10.1080/02786829808965551, 1998.

Andreae, M. O. and Gelencsér, A.: Black carbon or brown carbon? The nature of light-absorbing carbonaceous aerosols, Atmos. Chem. Phys., 6, 3131–3148, doi:10.5194/acp-6-3131-2006, 2006.

Bergin, M. H., Cass, G. R., Xu, J., Fang, C., Zeng, L. M., Yu, T., Salmon, L. G., Kiang, C. S., Tang, X. Y., Zhang, Y. H., and Chameides, W. L.: Aerosol radiative, physical, and chemical properties in Beijing during June 1999, J. Geophys. Res.-Atmos., 106, 17969–17980, doi:10.1029/2001jd900073, 2001.

Cao, J., Wang, Q., Chow, J. C., Watson, J. G., Tie, X., Shen, Z., Wang, P., and An, Z.: Impacts of aerosol compositions on visibility impairment in Xi'an, China, Atmos. Environ., 59, 559–566, doi:10.1016/j.atmosenv.2012.05.036, 2012.

Cappa, C. D., Che, D. L., Kessler, S. H., Kroll, J. H., and Wilson, K. R.: Variations in organic aerosol optical and hygroscopic properties upon heterogeneous OH oxidation, J. Geophys. Res.-Atmos., 116, D15204, doi:10.1029/2011jd015918, 2011.

ACPD

12, 31955–31990, 2012

Cappa, C. D., Onasch, T. B., Massoli, P., Worsnop, D. R., Bates, T. S., Cross, E. S., Davidovits, P., Hakala, J., Hayden, K. L., Jobson, B. T., Kolesar, K. R., Lack, D. A., Lerner, B. M., Li, S. M., Mellon, D., Nuaaman, I., Olfert, J. S., Petaja, T., Quinn, P. K., Song, C., Subramanian, R., Williams, E. J., and Zaveri, R. A.: Radiative Absorption Enhancements Due to the Mixing State of Atmospheric Black Carbon, Science, 337, 1078–1081, doi:10.1126/science.1223447, 2012.

Chan, C. K. and Yao, X.: Air pollution in mega cities in China, Atmos. Environ., 42, 1–42, doi:10.1016/j.atmosenv.2007.09.003, 2008.

Chow, J. C., Bachmann, J. D., Wierman, S. S. G., Mathai, C. V., Malm, W. C., White, W. H., Mueller, P. K., Kumar, N., and Watson, J. G.: Visibility: science and regulation, J. Air. Waste. Manage., 52, 973–999, doi:10.1080/10473289.2002.10470844, 2002a.

Chow, J. C., Watson, J. G., Lowenthal, D. H., and Richards, L. W.: Comparability between PM_2.5 and particle light scattering measurements, Environ. Monit. Assess., 79, 29–45, doi:10.1023/a:1020047307117, 2002b.

Denkenberger, K. A., Moffet, R. C., Holecek, J. C., Rebotier, T. P., and Prather, K. A.: Real-time, single-particle measurements of oligomers in aged ambient aerosol particles, Environ. Sci. Technol., 41, 5439–5446, doi:10.1021/es070329l, 2007.

Du, H. H., Kong, L. D., Cheng, T. T., Chen, J. M., Du, J. F., Li, L., Xia, X. G., Leng, C. P., and Huang, G. H.: Insights into summertime haze pollution events over Shanghai based on online water-soluble ionic composition of aerosols, Atmos. Environ., 45, 5131–5137, doi:10.1016/j.atmosenv.2011.06.027, 2011.

Gard, E., Mayer, J. E., Morrical, B. D., Dienes, T., Fergenson, D. P., and Prather, K. A.: Real-time analysis of individual atmospheric aerosol particles: Design and performance of a portable ATOFMS, Anal. Chem., 69, 4083–4091, doi:10.1021/ac970540n, 1997.

Harris, B. M. and Highwood, E. J.: A simple relationship between volcanic sulfate aerosol optical depth and surface temperature change simulated in an atmosphere-ocean general circulation model, J. Geophys. Res.-Atmos., 116, D05109, doi:10.1029/2010jd014581, 2011.

He, K., Zhao, Q., Ma, Y., Duan, F., Yang, F., Shi, Z., and Chen, G.: Spatial and seasonal variability of PM_2.5 acidity at two Chinese megacities: insights into the formation of secondary inorganic aerosols, Atmos. Chem. Phys., 12, 1377–1395, doi:10.5194/acp-12-1377-2012, 2012.

Huang, K., Zhuang, G., Lin, Y., Fu, J. S., Wang, Q., Liu, T., Zhang, R., Jiang, Y., Deng, C., Fu, Q., Hsu, N. C., and Cao, B.: Typical types and formation mechanisms of haze in an Eastern

ACPD
12, 31955–31990, 2012

Asia megacity, Shanghai, Atmos. Chem. Phys., 12, 105–124, doi:10.5194/acp-12-105-2012, 2012a.
Huang, X., Song, Y., Li, M. M., Li, J. F., Huo, Q., Cai, X. H., Zhu, T., Hu, M., and Zhang, H. S.: A high-resolution ammonia emission inventory in China, Global Biogeochem. Cy., 26, GB1030, doi:10.1029/2011gb004161, 2012b.
Huang, X. F., He, L. Y., Xue, L., Sun, T. L., Zeng, L. W., Gong, Z. H., Hu, M., and Zhu, T.: Highly time-resolved chemical characterization of atmospheric fine particles during 2010 Shanghai World Expo, Atmos. Chem. Phys., 12, 4897–4907, doi:10.5194/acp-12-4897-2012, 2012c.
Huang, Y., Chen, H., Wang, L., Yang, X., and Chen, J.: Single particle analysis of amines in ambient aerosol in Shanghai, Environ. Chem., 9, 202–210, doi:10.1071/en11145, 2012d.
Jacobson, M. Z.: Strong radiative heating due to the mixing state of black carbon in atmospheric aerosols, Nature, 409, 695–697, doi:10.1038/35055518, 2001.
Jimenez, J. L., Canagaratna, M. R., Donahue, N. M., Prevot, A. S. H., Zhang, Q., Kroll, J. H., DeCarlo, P. F., Allan, J. D., Coe, H., Ng, N. L., Aiken, A. C., Docherty, K. S., Ulbrich, I. M., Grieshop, A. P., Robinson, A. L., Duplissy, J., Smith, J. D., Wilson, K. R., Lanz, V. A., Hueglin, C., Sun, Y. L., Tian, J., Laaksonen, A., Raatikainen, T., Rautiainen, J., Vaattovaara, P., Ehn, M., Kulmala, M., Tomlinson, J. M., Collins, D. R., Cubison, M. J., Dunlea, E. J., Huffman, J. A., Onasch, T. B., Alfarra, M. R., Williams, P. I., Bower, K., Kondo, Y., Schneider, J., Drewnick, F., Borrmann, S., Weimer, S., Demerjian, K., Salcedo, D., Cottrell, L., Griffin, R., Takami, A., Miyoshi, T., Hatakeyama, S., Shimono, A., Sun, J. Y., Zhang, Y. M., Dzepina, K., Kimmel, J. R., Sueper, D., Jayne, J. T., Herndon, S. C., Trimborn, A. M., Williams, L. R., Wood, E. C., Middlebrook, A. M., Kolb, C. E., Baltensperger, U., and Worsnop, D. R.: Evolution of organic aerosols in the atmosphere, Science, 326, 1525–1529, doi:10.1126/science.1180353, 2009.
Jongejan, P. A. C., Bai, Y., Veltkamp, A. C., Wyers, G. P., and Slanina, J.: An automated field instrument for the determination of acidic gases in air, Int. J. Environ. Anal. Chem., 66, 241–251, doi:10.1080/03067319708028367, 1997.
Kanakidou, M., Seinfeld, J. H., Pandis, S. N., Barnes, I., Dentener, F. J., Facchini, M. C., Van Dingenen, R., Ervens, B., Nenes, A., Nielsen, C. J., Swietlicki, E., Putaud, J. P., Balkanski, Y., Fuzzi, S., Horth, J., Moortgat, G. K., Winterhalter, R., Myhre, C. E. L., Tsigaridis, K., Vignati, E., Stephanou, E. G., and Wilson, J.: Organic aerosol and global climate modelling: A review, Atmos. Chem. Phys., 5, 1053–1123, doi:10.5194/acp-5-1053-2005, 2005.

ACPD
12, 31955–31990, 2012

Kaufman, Y. J., Koren, I., Remer, L. A., Rosenfeld, D., and Rudich, Y.: The effect of smoke, dust, and pollution aerosol on shallow cloud development over the Atlantic Ocean, Proc. Natl. Acad. Sci., 102, 11207–11212, doi:10.1073/pnas.0505191102, 2005.

Kopp, R. E. and Mauzerall, D. L.: Assessing the climatic benefits of black carbon mitigation, Proc. Natl. Acad. Sci., 107, 11703–11708, doi:10.1073/pnas.0909605107, 2010.

Lelieveld, J., Berresheim, H., Borrmann, S., Crutzen, P. J., Dentener, F. J., Fischer, H., Feichter, J., Flatau, P. J., Heland, J., Holzinger, R., Korrmann, R., Lawrence, M. G., Levin, Z., Markowicz, K. M., Mihalopoulos, N., Minikin, A., Ramanathan, V., de Reus, M., Roelofs, G. J., Scheeren, H. A., Sciare, J., Schlager, H., Schultz, M., Siegmund, P., Steil, B., Stephanou, E. G., Stier, P., Traub, M., Warneke, C., Williams, J., and Ziereis, H.: Global air pollution crossroads over the Mediterranean, Science, 298, 794–799, doi:10.1126/science.1075457, 2002.

Li, H. Y., Han, Z. W., Cheng, T. T., Du, H. H., Kong, L. D., Chen, J. M., Zhang, R. J., and Wang, W. J.: Agricultural fire impacts on the air quality of Shanghai during summer harvesttime, Aerosol Air Qual. Res., 10, 95–101, doi:10.4209/aaqr.2009.08.0049, 2010.

Li, L., Chen, J. M., Chen, H., Yang, X., Tang, Y., and Zhang, R. Y.: Monitoring optical properties of aerosols with cavity ring-down spectroscopy, J. Aerosol. Sci., 42, 277–284, doi:10.1016/j.jaerosci.2011.02.001, 2011a.

Li, W. J., Zhou, S. Z., Wang, X. F., Xu, Z., Yuan, C., Yu, Y. C., Zhang, Q. Z., and Wang, W. X.: Integrated evaluation of aerosols from regional brown hazes over northern China in winter: Concentrations, sources, transformation, and mixing states, J. Geophys. Res.-Atmos., 116, D09301, doi:10.1029/2010jd015099, 2011b.

Li, Y., Ezell, M. J., and Finlayson-Pitts, B. J.: The impact of organic coatings on light scattering by sodium chloride particles, Atmos. Environ., 45, 4123–4132, doi:10.1016/j.atmosenv.2011.05.031, 2011c.

Liu, P., Ziemann, P. J., Kittelson, D. B., and McMurry, P. H.: Generating particle beams of controlled dimensions and divergence: I. Theory of particle motion in aerodynamic lenses and nozzle expansions, Aerosol Sci. Tech., 22, 293–313, doi:10.1080/02786829408959748, 1995a.

Liu, P., Ziemann, P. J., Kittelson, D. B., and McMurry, P. H.: Generating particle beams of controlled dimensions and divergence: II. Experimental evaluation of particle motion in aerodynamic lenses and nozzle expansions, Aerosol Sci. Tech., 22, 314–324, doi:10.1080/02786829408959749, 1995b.

ACPD
12, 31955–31990, 2012

Makkonen, U., Virkkula, A., Mäntykenttä, J., Hakola, H., Keronen, P., Vakkari, V., and Aalto, P. P.: Semi-continuous gas and inorganic aerosol measurements at a Finnish urban site: comparisons with filters, nitrogen in aerosol and gas phases, and aerosol acidity, Atmos. Chem. Phys., 12, 5617–5631, doi:10.5194/acp-12-5617-2012, 2012.

Maria, S. F., Russell, L. M., Gilles, M. K., and Myneni, S. C. B.: Organic aerosol growth mechanisms and their climate-forcing implications, Science, 306, 1921–1924, doi:10.1126/science.1103491, 2004.

Moffet, R. C. and Prather, K. A.: In-situ measurements of the mixing state and optical properties of soot with implications for radiative forcing estimates, Proc. Natl. Acad. Sci., 106, 11872–11877, doi:10.1073/pnas.0900040106, 2009.

Moffet, R. C., de Foy, B., Molina, L. T., Molina, M. J., and Prather, K. A.: Measurement of ambient aerosols in northern Mexico City by single particle mass spectrometry, Atmos. Chem. Phys., 8, 4499–4516, doi:10.5194/acp-8-4499-2008, 2008.

Monge, M. E., D'Anna, B., Mazri, L., Giroir-Fendler, A., Ammann, M., Donaldson, D. J., and George, C.: Light changes the atmospheric reactivity of soot, Proc. Natl. Acad. Sci., 107, 6605–6609, doi:10.1073/pnas.0908341107, 2010.

Murphy, D. M., Anderson, J. R., Quinn, P. K., McInnes, L. M., Brechtel, F. J., Kreidenweis, S. M., Middlebrook, A. M., Pósfai, M., Thomson, D. S., and Buseck, P. R.: Influence of sea-salt on aerosol radiative properties in the Southern Ocean marine boundary layer, Nature, 392, 62–65, doi:10.1038/32138, 1998.

Nguyen, T. B., Lee, P. B., Updyke, K. M., Bones, D. L., Laskin, J., Laskin, A., and Nizkorodov, S. A.: Formation of nitrogen- and sulfur-containing light-absorbing compounds accelerated by evaporation of water from secondary organic aerosols, J. Geophys. Res.-Atmos., 117, D01207, doi:10.1029/2011jd016944, 2012.

Pathak, R. K., Wu, W. S., and Wang, T.: Summertime PM2.5 ionic species in four major cities of China: Nitrate formation in an ammonia-deficient atmosphere, Atmos. Chem. Phys., 9, 1711–1722, doi:10.5194/acp-9-1711-2009, 2009.

Pratt, K. A. and Prather, K. A.: Mass spectrometry of atmospheric aerosols – Recent developments and applications, Part 2: On-line mass spectrometry techniques, Mass. Spectrom. Rev., 31, 17–48, doi:10.1002/mas.20330, 2012.

Pöschl, U.: Atmospheric aerosols: Composition, transformation, climate and health effects, Angew. Chem. Int. Ed., 44, 7520–7540, doi:10.1002/anie.200501122, 2005.

ACPD
12, 31955–31990, 2012

Ramanathan, V., Crutzen, P. J., Kiehl, J. T., and Rosenfeld, D.: Aerosols, climate, and the hydrological cycle, Science, 294, 2119–2124, doi:10.1126/science.1064034, 2001.
Robinson, A. L., Donahue, N. M., Shrivastava, M. K., Weitkamp, E. A., Sage, A. M., Grieshop, A. P., Lane, T. E., Pierce, J. R., and Pandis, S. N.: Rethinking organic aerosols: Semivolatile emissions and photochemical aging, Science, 315, 1259–1262, doi:10.1126/science.1133061, 2007.
Seinfeld, J. H. and Pandis, S. N.: Atmospheric Chemistry and Physics: From air pollution to climate change, John Wiley & Sons, New York, 1998.
Song, X. H., Hopke, P. K., Fergenson, D. P., and Prather, K. A.: Classification of single particles analyzed by ATOFMS using an artificial neural network, ART-2A, Anal. Chem., 71, 860–865, doi:10.1021/ac9809682, 1999.
Spencer, M. T. and Prather, K. A.: Using ATOFMS to determine OC/EC mass fractions in particles, Aerosol Sci. Tech., 40, 585–594, doi:10.1080/02786820600729138, 2006.
Sun, H. L., Biedermann, L., and Bond, T. C.: Color of brown carbon: A model for ultraviolet and visible light absorption by organic carbon aerosol, Geophys. Res. Lett., 34, L17813, doi:10.1029/2007gl029797, 2007.
Titos, G., Foyo-Moreno, I., Lyamani, H., Querol, X., Alastuey, A., and Alados-Arboledas, L.: Optical properties and chemical composition of aerosol particles at an urban location: An estimation of the aerosol mass scattering and absorption efficiencies, J. Geophys. Res.-Atmos., 117, D04206, doi:10.1029/2011jd016671, 2012.
Wang, K. C., Dickinson, R. E., and Liang, S. L.: Clear sky visibility has decreased over land globally from 1973 to 2007, Science, 323, 1468–1470, doi:10.1126/science.1167549, 2009a.
Wang, X. F., Zhang, Y. P., Chen, H., Yang, X., Chen, J. M., and Geng, F. H.: Particulate nitrate formation in a highly polluted urban area: A case study by single-particle mass spectrometry in Shanghai, Environ. Sci. Technol., 43, 3061–3066, doi:10.1021/es8020155, 2009b.
Wang, X. F., Gao, S., Yang, X., Chen, H., Chen, J. M., Zhuang, G. S., Surratt, J. D., Chan, M. N., and Seinfeld, J. H.: Evidence for high molecular weight nitrogen-containing organic salts in urban aerosols, Environ. Sci. Technol., 44, 4441–4446, doi:10.1021/es1001117, 2010.
Wang, X. M., Ding, X., Fu, X. X., He, Q. F., Wang, S. Y., Bernard, F., Zhao, X. Y., and Wu, D.: Aerosol scattering coefficients and major chemical compositions of fine particles observed at a rural site hit the central Pearl River Delta, South China, J. Environ. Sci.-China, 24, 72–77, doi:10.1016/s1001-0742(11)60730-4, 2012.

ACPD
12, 31955–31990, 2012

Wonaschütz, A., Hitzenberger, R., Bauer, H., Pouresmaeil, P., Klatzer, B., Caseiro, A., and Puxbaum, H.: Application of the integrating sphere method to separate the contributions of brown and black carbon in atmospheric aerosols, Environ. Sci. Technol., 43, 1141–1146, doi:10.1021/es8008503, 2009.

Yang, M., Howell, S. G., Zhuang, J., and Huebert, B. J.: Attribution of aerosol light absorption to black carbon, brown carbon, and dust in China – interpretations of atmospheric measurements during EAST-AIRE, Atmos. Chem. Phys., 9, 2035–2050, doi:10.5194/acp-9-2035-2009, 2009.

Yang, F., Chen, H., Du, J. F., Yang, X., Gao, S., Chen, J. M., and Geng, F. H.: Evolution of the mixing state of fine aerosols during haze events in Shanghai, Atmos. Res., 104, 193–201, doi:10.1016/j.atmosres.2011.10.005, 2012.

Zhang, R. Y., Khalizov, A. F., Pagels, J., Zhang, D., Xue, H. X., and McMurry, P. H.: Variability in morphology, hygroscopicity, and optical properties of soot aerosols during atmospheric processing, Proc. Natl. Acad. Sci., 105, 10291–10296, doi:10.1073/pnas.0804860105, 2008.

Zhang, F. W., Xu, L. L., Chen, J. S., Yu, Y. K., Niu, Z. C., and Yin, L. Q.: Chemical compositions and extinction coefficients of PM_2.5 in peri-urban of Xiamen, China, during June 2009–May 2010, Atmos. Res., 106, 150–158, doi:10.1016/j.atmosres.2011.12.005, 2012a.

Zhang, X. Y., Wang, Y. Q., Niu, T., Zhang, X. C., Gong, S. L., Zhang, Y. M., and Sun, J. Y.: Atmospheric aerosol compositions in China: spatial/temporal variability, chemical signature, regional haze distribution and comparisons with global aerosols, Atmos. Chem. Phys., 12, 779–799, doi:10.5194/acp-12-779-2012, 2012b.

ACPD
12, 31955–31990, 2012

Table 1. The names, start times, end times, and duration of the three periods and four sub-periods.

	Period 1	Period 2		Period 3
Start Time (local)	13 Oct 00:00	13 Oct 23:00		15 Oct 10:00
End Time (local)	13 Oct 23:00	15 Oct 10:00		16 Oct 00:00
Length (hour)	23	35		14
	Period 1a	Period 2a	Period 2b	Period 3a
Start Time (local)	13 Oct 00:00	14 Oct 00:00	14 Oct 18:00	15 Oct 12:00
End Time (local)	13 Oct 14:00	14 Oct 14:00	15 Oct 10:00	16 Oct 00:00
Length (hour)	14	14	16	12

ACPD
12, 31955–31990, 2012

Table 2. Names and fractions of the 11 particle types identified from the ATOFMS data.

Group	% of Particles
Fresh Biomass Burning (BB)	4.9
Aged Biomass Burning (BB)	17.5
Fresh Organic Carbon (OC)	12.0
Aged Organic Carbon (OC)	14.6
Fresh Elemental/Organic Carbon (ECOC)	4.8
Aged Elemental/Organic Carbon (ECOC)	3.9
Ammonium	19.3
Na-K-rich	3.6
Elemental Carbon (EC)	1.9
Dust	2.2
Metal	8.2
Total	92.9

ACPD
12, 31955–31990, 2012

Table 3. The correlation coefficient (R^2) between the extinction coefficient and mass concentration of PM_{10}, $PM_{2.5}$, and PM_1 in the three time periods.

	Period 1	Period 2	Period 3
PM_{10}	0.37	0.49	0.73
$PM_{2.5}$	0.57	0.58	0.92
PM_1	0.65	0.61	0.92

ACPD
12, 31955–31990, 2012

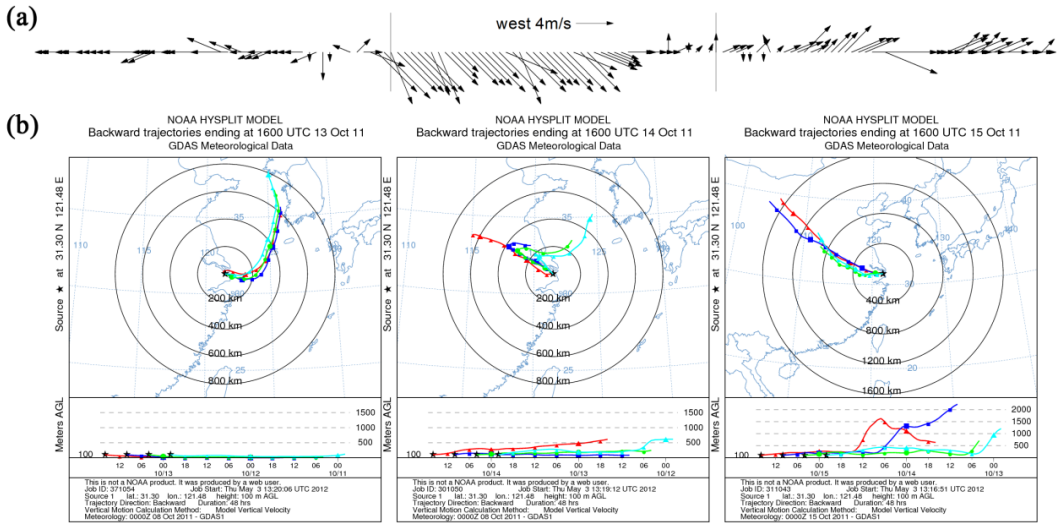

Fig. 1. (a) Temporal wind direction and speed on 13–15 October 2011. **(b)** Six-hourly resolved 48-h air mass back trajectories from 13, 14, and 15 October 2011.

ACPD
12, 31955–31990, 2012

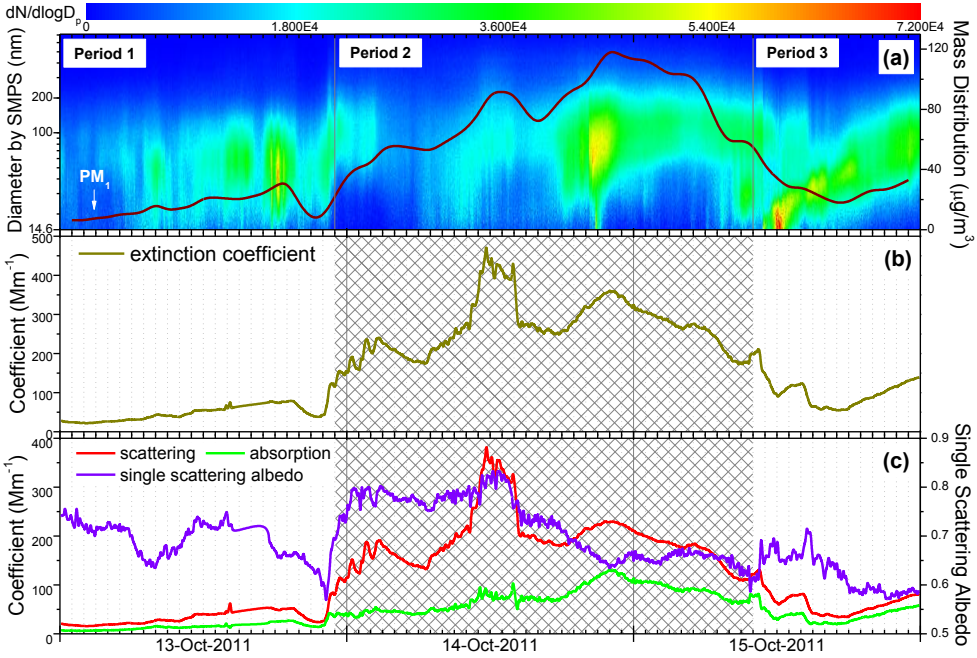

Fig. 2. (a) The number distribution detected by SMPS together with hourly average PM_1 mass concentration. **(b)** The extinction coefficient over the sampling period. **(c)** The scattering coefficient, absorption coefficient and single scattering albedo over the sampling period.

ACPD
12, 31955–31990, 2012

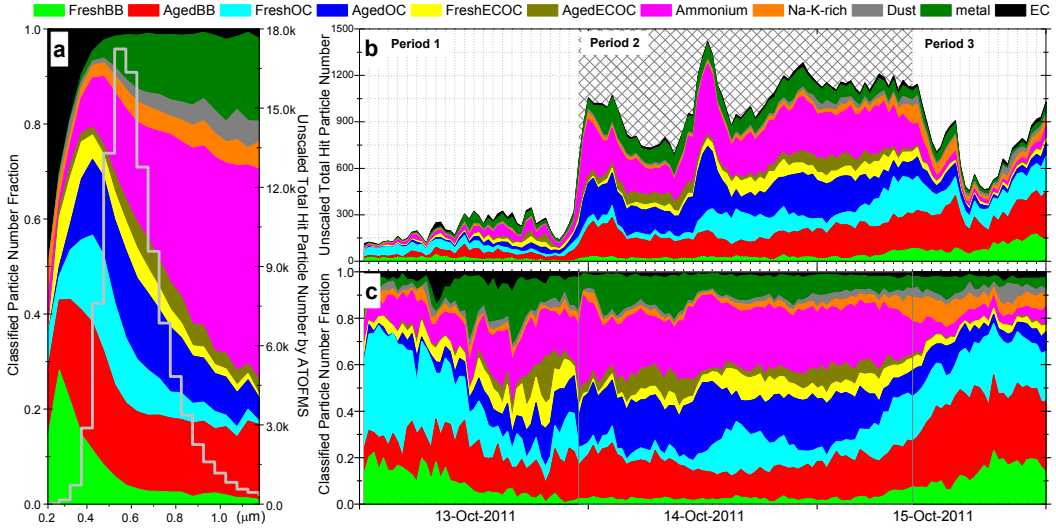

Fig. 3. (a) Chemically resolved size distributions of particle number fractions and the size distribution of unscaled total hit particle number by ATOFMS (gray line). **(b)** Temporal variation of different particle type counts with 30-min time resolution. **(c)** Temporal variation of number fractions of different particle types with 30-min time resolution.

ACPD
12, 31955–31990, 2012

A case study of the highly time-resolved evolution of aerosol chemical

Y. Huang et al.

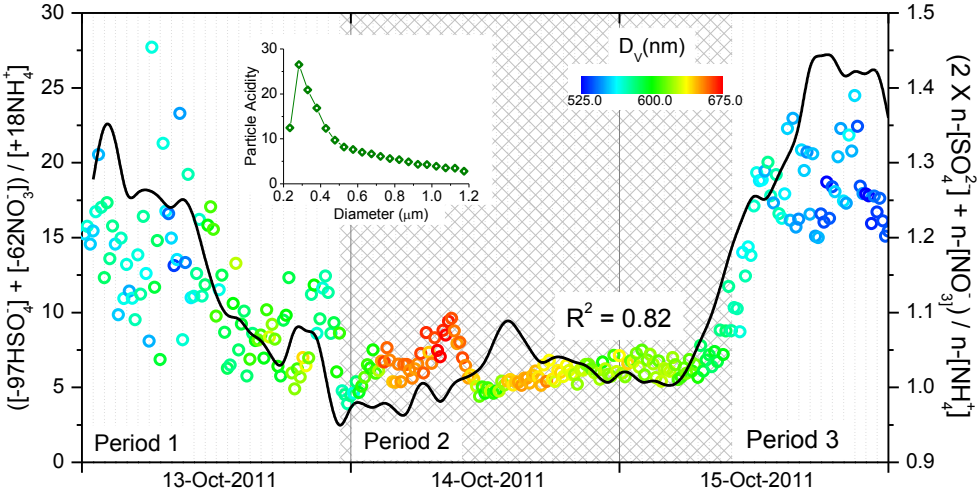

Fig. 4. Particle acidity plotted as a function of time from ATOFMS data with 15-min resolution (circles, left-hand y-axis). The color indicates the average aerodynamic diameter for particle in the 200–1200 nm size range detected by ATOFMS. The black line shows MARGA data for particle acidity (right-hand y-axis). The inset shows the size resolved particle acidity from ATOFMS data, averaged over the entire study.

ACPD
12, 31955–31990, 2012

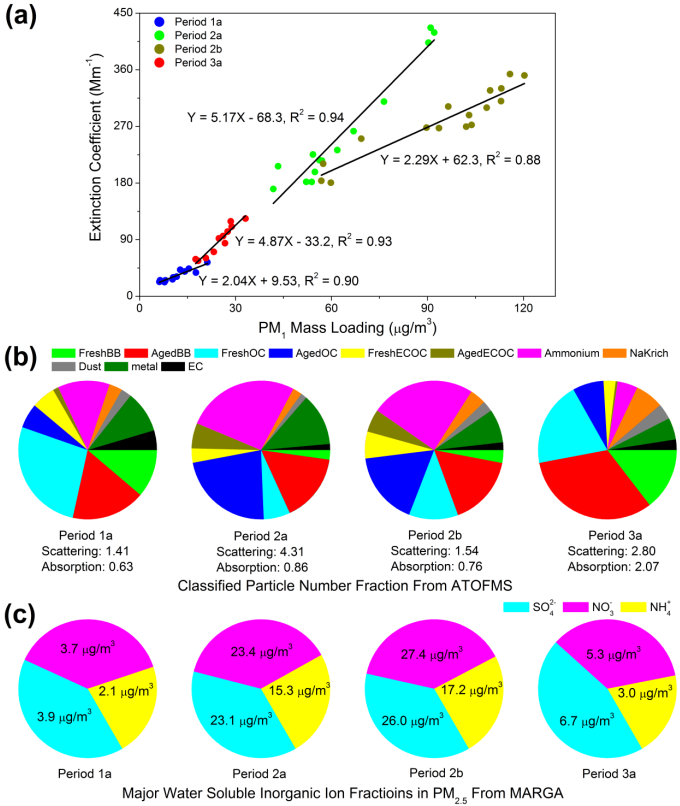

Fig. 5. (a) Extinction coefficient plotted versus PM_1 mass loading with linear fits in the four sub-periods. **(b)** Average chemically resolved fractions of different particle types from ATOFMS in the four sub-periods. **(c)** Distributions of water-soluble sulfate, nitrate, and ammonium mass concentrations in $PM_{2.5}$ from MARGA in the four sub-periods.

ACPD
12, 31955–31990, 2012